



Turbulent mixing controls fixation of growing antagonistic populations

Jonathan Bauermann^a, Roberto Benzi^{b,c}, David R. Nelson^{a,1} , Suraj Shankar^{a,d} , and Federico Toschi^{e,f}

Affiliations are included on p. 7.

Contributed by David R. Nelson; received August 21, 2024; accepted January 8, 2025; reviewed by Nigel Goldenfeld and Katepalli R. Sreenivasan

Unlike coffee and cream that homogenize when stirred, growing micro-organisms (e.g., bacteria, baker's yeast) can actively kill each other and avoid mixing. How do such antagonistic interactions impact the growth and survival of competing strains, while being spatially advected by turbulent flows? By using numerical simulations of a continuum model, we study the dynamics of two antagonistic strains that are dispersed by incompressible turbulent flows in two spatial dimensions. A key parameter is the ratio of the fluid transport time to that of biological reproduction, which determines the winning organism that ultimately takes over the whole population from an initial heterogeneous state, a process known as fixation. By quantifying the probability and mean time for fixation along with the spatial structure of concentration fluctuations, we demonstrate how turbulence raises the threshold for biological nucleation and antagonism suppresses flow-induced mixing by depleting the population at interfaces. Our work highlights the unusual biological consequences of the interplay of turbulent fluid flows with antagonistic population dynamics, with potential implications for marine microbial ecology and origins of biological chirality.

spatial population dynamics | antagonism | nonreciprocal interactions | turbulent mixing

Life in the ocean is responsible for sustaining global ecological and geophysical processes, such as the carbon cycle, of which marine phytoplankton are the primary drivers of this energy and mass flux (1). The growth of these microorganisms occurs in a complex and dynamic fluid environment, naturally raising the question of how turbulent flows impact their spatial distribution (2). That turbulent flows near the ocean surface can generate patchy spatial patterns (3), create transient hydrodynamical niches (4, 5), and enable coexistence of diverse phytoplankton populations has been recognized across a wide range of spatial (1 to 100 km) and temporal (~days to months) scales (4–9). But how these hydrodynamic processes combine with biological interactions between growing communities of distinct microbes remains a challenging open question.

Previous studies have investigated the role of both dynamic and static fluid flows on growing, competing populations (2, 10–12) with a focus on compressible effects that can strongly suppress the carrying capacity (10) and modify the effective selective advantage of the population (13, 14). While compressible effects are important on the submesoscale (~1 to 10 km spatial scale) due to strong horizontal flow divergence (3, 14), on larger scales ≥ 10 km, flows are approximately two-dimensional (2D) and incompressible. Furthermore, phytoplankton often exhibit asymmetric and antagonistic interactions, e.g., between bacteria and toxic algae or phages (15–17), that cause competing organisms to actively attack, poison, or kill one another. In spatial settings, such antagonism leads to a novel kind of active matter (18) with segregated domains and a genetic line tension that prevents intermingling of the different populations (19, 20). As a result, a biological nucleation process, rather than simple Darwinian selective advantage, governs the fixation or extinction of either population, as has been recently demonstrated for antagonistic strains of *Saccharomyces cerevisiae* (baker's yeast) competing on a Petri dish (21).

Here, we combine fluid dynamics with spatial population genetics of a simple reaction–diffusion model to study the role of turbulent mixing on fixation of antagonistically interacting organisms. The combination of both processes, turbulent mixing and the population dynamics of antagonistic organisms, yields an unusual setting of constantly stirring a genetic mixture that tries to actively demix by itself, influenced by a genetic line tension (21). This transient dynamics terminates when one of the strains takes over the entire population and achieves genetic fixation. Remarkably, which organism finally wins depends strongly on the strength of turbulent mixing which shears the mixture; creating more biological interfaces with antagonism depletes the population. We develop

Significance

From microbes to mammals, living organisms experience conflict and predation, causing their populations to segregate with antagonistic interactions. Similar interactions govern patterns in chemical mixtures, e.g., chiral synthesis. But how does this spatial organization occur in dynamic environments like turbulent flow? Through simulations and analysis, we demonstrate how antagonism suppresses turbulent mixing and how fluid flow controls extinction dynamics in a mixture of proliferating, antagonistic organisms. Survival of a droplet of fitter organisms proceeds via a biological nucleation process whose threshold is dramatically modified by fluid mixing. Our work provides a quantitative and predictive framework to understand how fluid turbulence impacts spatial population dynamics with nonreciprocal interactions, and suggests experimental tests of the results.

Reviewers: N.G., University of California, San Diego; and K.R.S., New York University.

The authors declare no competing interest.

Copyright © 2025 the Author(s). Published by PNAS. This open access article is distributed under [Creative Commons Attribution-NonCommercial-NoDerivatives License 4.0 \(CC BY-NC-ND\)](#).

¹To whom correspondence may be addressed. Email: drnelson@fas.harvard.edu.

This article contains supporting information online at <https://www.pnas.org/lookup/suppl/doi:10.1073/pnas.2417075122/-DCSupplemental>.

Published February 14, 2025.

an analytical model for the flow-modified nucleation process, and quantitatively test its predictions with our numerical results. Finally, we compute the spatial spectrum of concentration fluctuations and compare them with other phase-separating systems. We conclude by suggesting potential experimental tests and highlighting the implications of our results for biological and chemical systems.

Reaction–Diffusion Model for Turbulent Antagonism

Following previous studies we adopt a continuum description that neglects demographic noise (22) and models the population dynamics in 2D as (2)

$$(\partial_t + \mathbf{v} \cdot \nabla) c_A = D \nabla^2 c_A + \mu c_A (1 - c_A - c_B + \alpha c_B), \quad [1]$$

$$(\partial_t + \mathbf{v} \cdot \nabla) c_B = D \nabla^2 c_B + \mu c_B (1 - c_A - c_B + \beta c_A), \quad [2]$$

where $c_A(\mathbf{x}, t)$, $c_B(\mathbf{x}, t)$ are the local concentrations of the two populations (A , B) advected by a 2D incompressible turbulent flow field $\mathbf{v}(\mathbf{x}, t)$ along with an effective diffusivity D . The initial growth rate of both strains is assumed to have a common value μ for simplicity, and α , β parameterize the interactions between strains. Below we will simply refer to A , B as “strains” given their common individual reproductive and transport characteristics, though Eqs. 1 and 2 are simply an advective extension of generalized Lotka–Volterra models used more broadly to describe interacting species, predator–prey competition, and pattern formation in a wide variety of ecological contexts (23, 24). We will focus on the case where $\alpha < 0$ and $\beta < 0$ corresponding to antagonism (20). Note that these interactions are nonreciprocal for all asymmetric settings $\alpha \neq \beta$.

The 2D flow field $\mathbf{v}(\mathbf{x}, t)$ is obtained by considering the evolution of 2D slices of three-dimensional (3D), homogeneous, and isotropic turbulent flow generated from direct numerical simulations of the Navier–Stokes equation and retaining only the incompressible part (see *SI Appendix* for details). Because our velocity field is generated from 3D flows, we subject our strains to simple direct turbulence cascades, and neglect complications due to inverse or enstrophy cascades (25). For simplicity, we ignore any feedback from the concentration fields on the hydrodynamic flows and consider equal diffusion constants for both strains, leaving the study of these interesting effects for the future.

Stirred turbulent flows of a typical strength v_{rms} (the RMS velocity) on the scale of the system size L are controlled by the Reynolds number $\text{Re} = v_{\text{rms}} L / \nu$, where ν is the kinematic viscosity of the fluid. We restrict ourselves to a Reynolds number of $\text{Re} \approx 100$ in all the calculations in this work for reasons of computational efficiency. Upon comparing the large eddy turnover time $\tau_{\text{eddy}} = L / v_{\text{rms}}$ (26) with the time scale of reproduction ($1/\mu$), we obtain a key dimensionless number, the Damköhler number (27)

$$\text{Da} = \frac{\mu L}{v_{\text{rms}}}, \quad [3]$$

which controls the relative importance of hydrodynamic transport to biological growth. The strength of diffusion in population dynamics can be compared to fluid transport either via viscous diffusion (in terms of a Schmidt number $\text{Sc} = \nu / D$) or advection (in terms of a Péclet number, $\text{Pe} = v_{\text{rms}} L / D = \text{Re} \text{Sc}$). In this study, we vary the Damköhler number (Da) by varying the hydrodynamic time scale τ_{eddy} and thus, v_{rms} , while keeping the Reynolds number (Re) and key spatial scales constant; see

SI Appendix section 1 for details. As a consequence, however, the Schmidt number increases as $\text{Sc} = 0.1$ to 10 when the Damköhler number is varied from $\text{Da} = 0.1$ to 10.

To gain analytical insight into the population dynamics, it is useful to rewrite the model (Eqs. 1 and 2) in terms of the total concentration of both strains $c_T = c_A + c_B$ and the relative fraction of the A strain $f = c_A / c_T$ (2), which gives

$$(\partial_t + \mathbf{v} \cdot \nabla) c_T = D \nabla^2 c_T + \mu c_T [1 - c_T - 2\sigma c_T f (1 - f)], \quad [4]$$

$$(\partial_t + \mathbf{v} \cdot \nabla) f = D \nabla^2 f + \frac{2D}{c_T} \nabla c_T \cdot \nabla f + \mu c_T f (1 - f) \left[\frac{\delta}{2} + \sigma (2f - 1) \right]. \quad [5]$$

The selective advantage $\delta = \alpha - \beta$ quantifies the growth rate difference between the strains, i.e., for $\delta \geq 0$ strain A has a reproductive advantage/disadvantage over the strain B , while the nature of the interactions is quantified by $\sigma = -(\alpha + \beta)/2$ ($\sigma < 0$: mutualistic, $\sigma = 0$: neutral, $\sigma > 0$: antagonistic). Here, we focus on the antagonistic case and choose $\sigma > 0$, $\delta > 0$.

One advantage of this parameterization is that for weak enough antagonism, i.e., $\sigma \ll 1$, the total concentration is approximately $c_T \approx 1$ in incompressible flows ($\nabla \cdot \mathbf{v} = 0$) (2). In this limit, Eq. 5 reduces to an advected version of the dynamics of a nonconserved order parameter, so-called Model A dynamics in the classification of Hohenberg and Halperin (28). Unlike the more common setting of a conserved order parameter coupled to fluid flow (Model H) (28) or driven by turbulence (advected Model B) (29–31), e.g., stirring oil and water, the turbulent mixing of a nonconserved order parameter is unusual in condensed matter, as Model A typically describes the dynamics of magnets, which usually lose their magnetism before becoming liquid.

In Fig. 1, we compare the turbulent mixing of a passive scalar (e.g., “milk in coffee,” Fig. 1A and *Movie S1*), two antagonistic strains with $\delta = 0.1$ (blue has a selective advantage), $\sigma = 0.25$ and varying Damköhler number (Fig. 1B and *Movie S1*), and a phase-separating conserved order parameter (e.g., “oil in water,” Fig. 1C and *Movie S1*). In all cases, the advecting velocity field and initialization is the same, and it satisfies periodic boundary conditions in the $L \times L$ box. The dynamic patterns obtained are shown at identical time points (in units of τ_{eddy}). As a result, the early time dynamics (second and third column, Fig. 1) look similar in all five cases.

However, after the initial transient, the freely diffusing scalar loses all visible structures and reaches a well-mixed state (orange, Fig. 1A); see, for, e.g., ref. 32 for a perspective on the physics of turbulent mixing. Similarly, for low Damköhler numbers ($\text{Da} = 0.1$, first row in Fig. 1B), the initial circle of the blue strain gets quickly stirred into the surroundings and loses all visible structure, leading to a well-mixed state with $f = 0$ (red), despite the selective advantage of the blue strain. Weaker fluid transport ($\text{Da} = 5$) eventually allows the selectively favored strain to win, as the initial circle maintains its interfacial integrity while being constantly folded and stirred. In contrast, advected model B dynamics generates phase-separated domains that are broken up by turbulent mixing (Fig. 1C), leading to arrested coarsening of drops at the so-called Hinze scale (31, 33). Crucially, unlike the examples with conserved concentrations (Fig. 1A and C), in the nonconserved system (Fig. 1B), one of the strains always wins and achieves fixation at long times by filling the whole domain—the final states associated with Eqs. 1 and 2 are thus an absorbing boundary condition at long times!

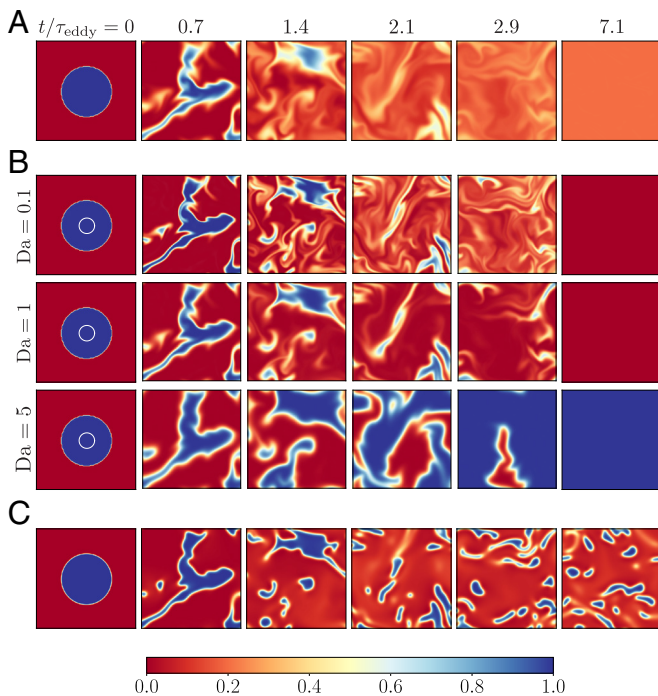


Fig. 1. Snapshots of the concentration field of a passive scalar in (A), the field of fraction f for different Damköhler numbers in (B), and the concentration field of a binary phase-separating mixture in (C) under turbulent mixing. All systems are stirred with the same turbulent flow field and shown at the same time points measured in units of the large eddy turnover time (τ_{eddy}). Additionally, we show the critical nucleation radius (white circle) in (B) in the absence of flow. Due to the identical initialization and flow fields, the structures formed in the early times (second and third column) look similar between all three processes. In all systems, we use a circular initialization that covers 20% of the system size (blue circle/first column). In (A) and (C), we show the concentration fields for a freely diffusing and advected passive scalar (“milk”) and a scalar following model B with advection (“oil”).

These examples demonstrate another key result—the Damköhler number, and thus turbulent mixing, controls which strain outcompetes the other at fixed initial fractions and can override the selective advantage. Below, we construct an analytical model to explain these results and test our predictions using numerical simulations.

Critical Fraction for Fixation Under Growth and Mixing

To understand how turbulent flows affect the criteria for fixation, we first consider two limiting cases. When turbulent mixing is much faster than biological reproduction ($\text{Da} \approx 0$), the system rapidly becomes spatially homogeneous, i.e., the dynamics is effectively zero-dimensional. In this limit, setting $c_T \approx 1$ ($\sigma \ll 1$), we find that the dynamics of f (Eq. 5) has two stable fixed points at $f = 0, 1$ and an unstable fixed point

$$f_c^0 = \frac{2\sigma - \delta}{4\sigma}, \quad [6]$$

that sets the critical fraction required for fixation of strain A (19, 20).

In the opposite limit of vanishing flow ($\text{Da} = \infty$), we neglect advection in Eq. 5 and obtain the classical dynamics of model A (with $c_T \approx 1$). The spatial dynamics of invasion is now governed by a pushed genetic wave that connects domains of strain B ($f = 0$) and strain A ($f = 1$) with an interface width $w = 2\sqrt{D/(\mu\sigma)}$

and speed $v_p = (\delta/2)\sqrt{D\mu/\sigma}$ (24, 34). As antagonism penalizes the contact between the two strains, the interface has an effective line tension $\gamma = (1/6)\sqrt{D\mu\sigma}$ (in 2D) (19, 20) that leads to a nucleation barrier, and thus minimal domain size, required for a strain with selective advantage to colonize a less fit population. To see this, consider the dynamics of a circular domain of radius R with a sharp interface ($w \ll R$) (2),

$$\frac{dR}{dt} = -\frac{D}{R} + v_p, \quad [7]$$

which (upon neglecting the periodic boundary conditions) defines the critical nucleation threshold $R_c^\infty = (2/\delta)\sqrt{D\sigma/\mu}$ in the absence of mixing. In a system of size L , this yields a critical fraction (area fraction in the system: $f = \pi R^2/L^2$) for invasion to be

$$f_c^\infty = \frac{4\pi\sigma D}{\mu\delta^2 L^2}, \quad [8]$$

in the limit of $\text{Da} = \infty$.

Motivated by the observations in Fig. 1, we minimally combine the two limits for arbitrary Da . We assume that at early times, with respect to the eddy turnover time, fluid shear is unlikely to destroy spatial structures, and at late times, turbulent mixing effectively homogenizes the population. We neglect scale-dependent fluctuations of the flow and quantify mixing by a single characteristic time scale

$$t_{\text{mix}} = \alpha\tau_{\text{eddy}}, \quad [9]$$

where the dimensionless parameter α , which we expect to be of order unity, captures the effectiveness of turbulent mixing and can depend on biological parameters. Thus an initial circular domain of size R_0 is assumed to grow or shrink via a pushed wave (Eq. 7) for $t < t_{\text{mix}}$, while for $t > t_{\text{mix}}$, the population is considered completely mixed with f_c^0 (Eq. 6) now determining which strain reaches fixation.

Direct integration of Eq. 7 yields

$$R(t, R_0) = R_c^\infty \left[1 + W_0 \left(\left(\frac{R_0}{R_c^\infty} - 1 \right) e^{\left(\frac{R_0 + v_p t}{R_c^\infty} - 1 \right)} \right) \right], \quad [10]$$

as the domain radius at time t , where $W_0(x)$ is the principal branch of Lambert W -function. Note that for $R_0/R_c^\infty < 1$, the initial domain is below the nucleation threshold, and extinction occurs in a finite time t_{ext} given by $t_{\text{ext}} = (R_c^\infty/v_p)[-\ln(1 - R_0/R_c^\infty) - R_0/R_c^\infty]$. Upon evaluating Eq. 10 for $t = t_{\text{mix}} = \alpha\tau_{\text{eddy}}$, we can obtain the critical size threshold R_c for the initial domain as an implicit relation

$$f_c^0 = \frac{\pi R(t_{\text{mix}}, R_c)^2}{L^2}. \quad [11]$$

To convert the critical domain size R_c into a critical fraction, we use $f_c = \pi R_c^2/L^2$ and solve for f_c to find

$$f_c = f_c^\infty \times \left[1 + W_0 \left(\left(\sqrt{\frac{f_c^0}{f_c^\infty}} - 1 \right) e^{\left(\sqrt{\frac{f_c^0}{f_c^\infty}} - 1 - \frac{v_p^2 t_{\text{mix}}}{D} \right)} \right) \right]^2. \quad [12]$$

Note that due to the definition of the Lambert W -function, $W_0(\exp(\sqrt{f_c^0/f_c^\infty} - 1)(\sqrt{f_c^0/f_c^\infty} - 1)) = \sqrt{f_c^0/f_c^\infty} - 1$ when

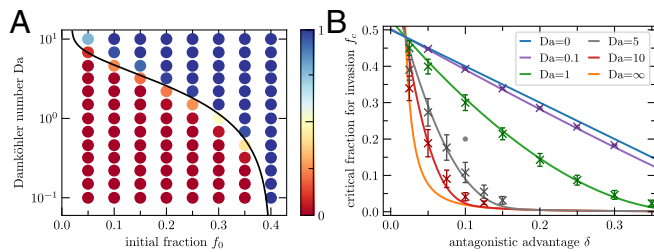


Fig. 2. The impact of turbulent flows on the fixation threshold. (A) The fraction at fixation (averaged over $N = 50$ runs) for different flow fields as a function of initial fractions f_0 and Damköhler numbers with $\delta = 0.1$ and $\sigma = 0.25$. The solid line is obtained from Eq. 12. Here, the factor α in the mixing time is obtained by fitting Eq. 12 (solid lines) to the numerically measured f_c in (B). Furthermore we show f_c^∞ (Eq. 6) and f_c^0 (Eq. 8) as function of δ . The gray dot denotes the parameter setting of Fig. 1, predicting the transition of fixation between $Da = 1$ and $Da = 5$.

$t_{\text{mix}} = 0$, thus $f_c = f_c^0$ in this limit ($Da = 0$). On the other hand, when $t_{\text{mix}} = \infty$ ($Da = \infty$), $W_0(0) = 0$, thus $f_c = f_c^\infty$.

To test the validity and usefulness of this simplified theoretical model, we run numerical simulations of the continuum dynamics (Eqs. 1 and 2) for $\delta = 0.1$, $\sigma = 0.25$ and construct a phase diagram showing the final fraction at fixation for varying Da and initial fractions f_0 of strain A inoculated in the system (Fig. 2A). For low Damköhler numbers ($Da \rightarrow 0$), the invading species achieves fixation only when the initial fraction $f_0 \geq f_c^0 \approx 0.4$, but as Da increases, the critical fraction for invasion decreases sharply until it reaches $f_c \approx f_c^\infty$. By averaging over $N = 50$ runs, we compute the probability of fixation as a sigmoidal function of the selective advantage and identify the critical fraction f_c from the inflection point (see SI Appendix, section 2 and Fig. S1 for details). Fig. 2B shows how the critical fraction needed for fixation of strain A varies with selective advantage δ , for different values of Da . As expected, f_c decreases as δ increases.

Remarkably, our analytical prediction of the critical fraction Eq. 12 agrees quantitatively with the numerical results (solid lines in Fig. 2), with just a single parameter $\alpha = 3.4 \pm 0.2$ that we fit for across all Damköhler numbers. That $\alpha > 1$ highlights the fact that antagonistic mixtures take significantly longer than freely diffusing scalars to get mixed by turbulence; the latter typically mix within one large eddy turnover time (26).

Clearly, the simple analytical argument of initial growth followed by instantaneous mixing is a huge simplification of the real dynamics in these mixtures. Nevertheless, the overall shape of Eq. 12 predicts the critical fraction for invasion effectively. Furthermore, we can predict the change in fixation probability between the two strains in Fig. 2A quantitatively (black line), given the value of α . Although the analysis uses an initial circular geometry, our predictions and results are robust to different initial conditions (see SI Appendix for details), highlighting the general validity of our theoretical framework.

Fixation Time and Mixing Time

Motivated by the success of our analytical model, we now use it to predict the dynamics of the system. In addition to the hydrodynamically important mixing time t_{mix} , a dynamical observable of considerable biological interest is the average fixation time t_{fix} , i.e., the time taken for either strain to reach fixation. As we have a continuum model, it is necessary to define a criterion of fixation or conversely, extinction. We set the threshold for extinction to be when the global average of the dying strain is less than $\epsilon = 10^{-7}$. Our results are insensitive

to this cutoff as long as the time for individuals to reproduce exceeds the diffusion time out of a local volume defined by the extinction cutoff (35).

We measure the fixation time in numerical simulations of Eqs. 1 and 2 for different flow fields. Fig. 3A shows the average fixation time t_{fix} (over $N = 250$ runs) in units of the biological time scale $1/\mu$, for $\delta = 0.1$, $\sigma = 0.25$ and varying flow fields (Da) and initial fractions (f_0). In all cases, smaller Damköhler numbers (i.e., stronger mixing) lead to shorter times for one species to reach fixation in the biological time scale. Close to the critical fraction ($f_0 \approx f_c^0$), the mean fixation time reaches a sharp maximum and displays strong sample-to-sample fluctuations for low initial fractions and larger Damköhler numbers ($Da = 5, 10$).

To understand these results, we adapt our previous theoretical arguments and estimate the fixation time in two steps (with $c_T \approx 1$). After one mixing time ($t = t_{\text{mix}}$), an initial fraction f_0 corresponding to a domain of size R_0 , evolves to $f^\infty(t_{\text{mix}}, f_0) = \pi R(t_{\text{mix}}, R_0)^2 / L^2$. The population is then assumed to be well-mixed for $t > t_{\text{mix}}$. Upon integrating Eq. 5 without spatial gradients, we obtain

$$t^0(f, f^\infty) = \frac{2}{\mu} \times \frac{(\delta + 2\sigma) \ln\left(\frac{1-f}{1-f^\infty}\right) - 4\delta \ln\left(\frac{\delta + 2\sigma(f-1)}{\delta + 2\sigma(f^\infty-1)}\right) - (\delta - 2\sigma) \ln\left(\frac{f}{f^\infty}\right)}{\delta^2 - 4\sigma^2}, \quad [13]$$

for the time it takes a starting fraction f^∞ to reach f . We assume $|\delta| < 2\sigma$, thus avoiding the spinodal lines for this phase separation problem at $\alpha = 0$ and $\beta = 0$. By taking into account which strain goes to fixation depending on the critical fraction, we combine these results to obtain the fixation time as

$$t_{\text{fix}} = \begin{cases} t_{\text{mix}} + t^0(\epsilon, f^\infty(t_{\text{mix}}, f_0)), & \text{if } f^\infty(t_{\text{mix}}, f_0) < f_c^0 \\ t_{\text{mix}} + t^0(1 - \epsilon, f^\infty(t_{\text{mix}}, f_0)), & \text{otherwise} \end{cases} \quad [14]$$

We plot the predicted fixation time (Eq. 14) in Fig. 3A (solid curves) and find excellent agreement for $Da \leq 1$ with no free parameters (α is obtained from the fits for the critical fraction; see Fig. 2). Interestingly, the dynamics for $Da > 1$ and $Da \leq 1$ are qualitatively different. In the latter case, mixing is sufficiently strong for antagonism to delay fixation. As a result, the measured $t_{\text{fix}} > t_{\text{mix}}$ (t_{mix} is indicated by the dashed horizontal lines according to the Damköhler numbers in Fig. 3A, and our analytical prediction (Eq. 14) gets better over a wide range of initial fractions f_0 , as the Damköhler number decreases. Furthermore, our numerical results also show the highest fixation times close to the critical fraction of fixation, as predicted by the logarithmic divergence in Eq. 14. These times result because for low Damköhler numbers f is well mixed and close to the unstable fixed point f_c^0 . In contrast, for larger Damköhler numbers ($Da > 1$), fixation occurs quickly with the measured $t_{\text{fix}} < t_{\text{mix}}$, which our analytical result (Eq. 14) fails to capture. In this regime, fluctuations in the flow become important for the dynamics, especially near the critical fraction, and our approximation of a single mixing timescale breaks down.

To better understand these fluctuations and their impact on the fixation time, we show a histogram ($N = 500$ different runs) of fixation times for $Da = 10$ ($f_0 = 0.05$) in the main panel of Fig. 3B. Interestingly, in this case, we find a bimodal distribution with a smaller peak for much lower fixation times than compared to the second peak, which is spread around the prediction from Eq. 14 (dashed vertical line). Furthermore, there exist some rare

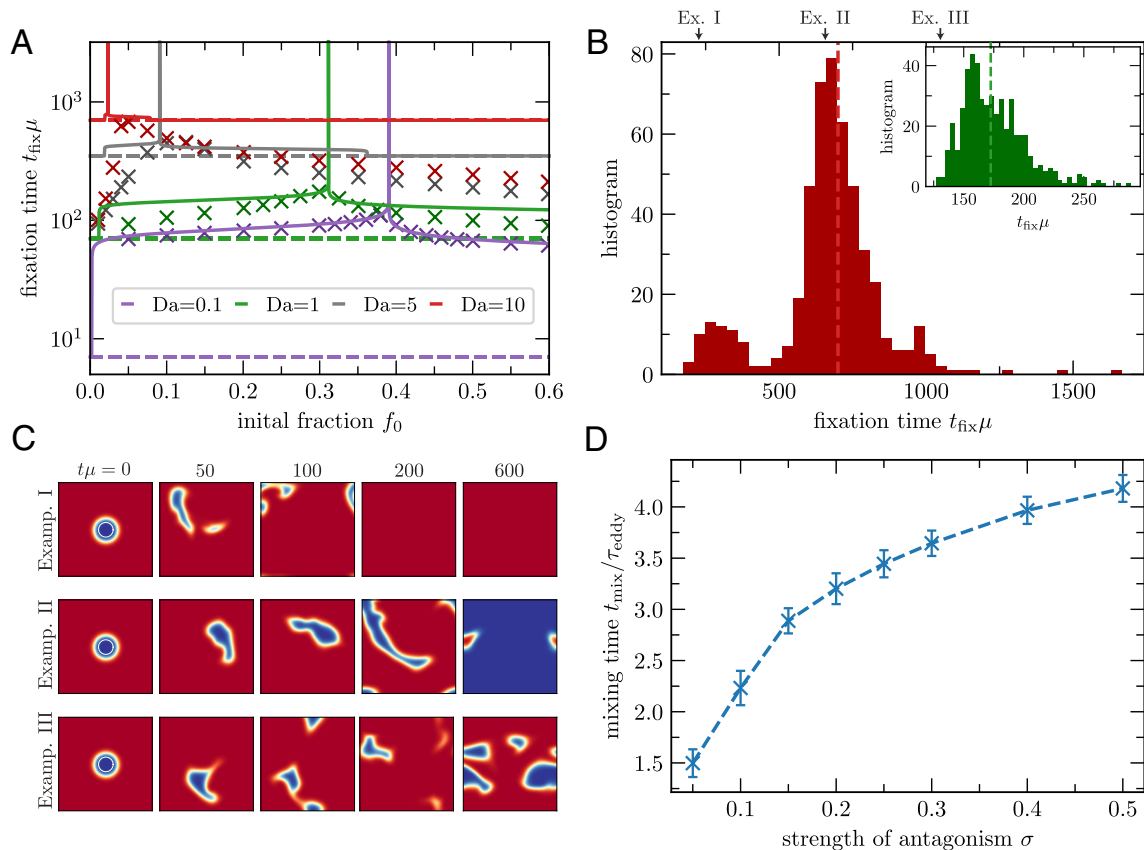


Fig. 3. Fixation time as a function of the initial fraction f_0 for different Damköhler numbers in units of the biological time scale $1/\mu$ (A). Points are obtained via the sample mean of $N = 250$ runs with their corresponding SE. Solid lines follow Eq. 14. Dashed lines indicate corresponding mixing times t_{mix} . In (B), we show the histogram of fixation times for $N = 500$ runs for $\text{Da} = 10, f_0 = 0.05$, and $\text{Da} = 1, f_0 = 0.3$ in the *Inset*. In (C), we show spatial snapshots of the fraction under different flow fields for $\text{Da} = 10, f_0 = 0.05$. Measured mixing times as a function of σ are shown in (D).

events of extreme long fixation times. Both of these features are absent in the histogram of fixation times for $\text{Da} = 1$ ($f_0 = 0.3$), shown in the *Inset* of Fig. 3B. Here, we find a single peak around the predicted time (via Eq. 14, indicated by the dashed vertical line). Remarkably, for $\text{Da} > 1$, our analytical approach is able to capture the most probable fixation time, rather than the average, as shown in the main panel of Fig. 3B.

We show snapshots of the dynamics for three different flow realizations in Fig. 3C at $\text{Da} = 10$, and indicate their fixation time on top of Fig. 3B. In some cases, the advected domains get stretched and quickly split below their critical nucleation radius (indicated by the white circle), allowing strain B to immediately fix (see Fig. 3B, Examp. I; first row). In other cases, intermittent fluctuations in the flow remain weak enough to only deform the domains a little; providing strain A sufficient time to grow and invade the system (see Fig. 3B, Examp. II; second row). In still other cases, consecutive splitting, and partial extinction events can maintain drops of the invading strain close to the critical size, causing a dramatic increase in the fixation time (see Fig. 3B, Examp. III; third row). All these different scenarios lead to the broad range of fixation times for high Damköhler numbers. In some cases, with relatively low probability, the biological reproduction is fast enough to keep the integrity of domain interfaces, and thereby preventing mixing. For such domains, fixation can now happen on a time scale below the mixing time, set by a pushed-wave dynamics of these interfaces, and the homogenizing effect of mixing gets lost. Therefore, in these cases, the specific flow fields matter much more for the fate of a domain.

Finally, we address the dependence of the mixing time (t_{mix}) on biological antagonism (σ). Intriguingly, we find that the measured t_{mix} (obtained by fitting for the critical fraction as in Fig. 2B) increases with antagonism (Fig. 3D). An order of magnitude increase in σ (from 0.05 to 0.5) leads to a nearly threefold increase in the mixing time, quantifying our intuition that antagonism makes mixing by stirring harder.

Concentration Spectra Under Turbulent Mixing

So far, we focused mainly on the global dynamics of the system. We now quantify spatial fluctuations of the competing populations and draw comparisons with classical studies of turbulent passive scalars or phase-separating mixtures (29–31, 36).

We measure the shell-averaged concentration spectrum normalized by the corresponding structure function $S(k_n) = (\sum_{k_n} |\hat{f}(\mathbf{k}, t)|^2) / (\sum_{k_n} 1)$, where $\hat{f}(\mathbf{k}, t)$ is the Fourier transform of the fraction $f(\mathbf{x}, t)$ and \sum_{k_n} denotes the sum over all modes within the n 'th shell, i.e., a mode with modulus $k = |\mathbf{k}|$ lies in the n 'th shell when $k \in [k_0 b^{n-1/2}, k_0 b^{n+1/2}]$, where b is a discretization parameter and $k_0 = 1/L$ (smallest mode). We choose $b = 1.14$, such that we obtain roughly five shells per octave. We similarly compute the conventional energy spectrum $E(k)$ of fluid turbulence (26).

Fig. 4A shows the stationary state of the energy spectrum for our 2D incompressible, turbulent flow field, along with the Kolmogorov scaling $E(k) \propto k^{-5/3}$, indicated as a straight line.

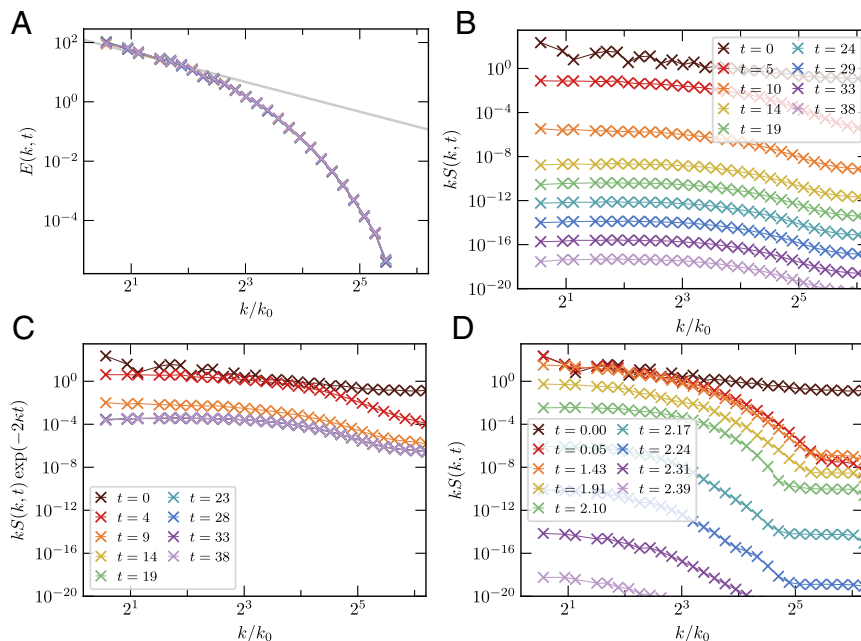


Fig. 4. Spatial fluctuations of turbulent population dynamics. (A) Steady state shell averaged spectrum at of the kinetic energy computed from the turbulent flow field (straight line show Kolmogorov scaling, $E(k) \propto k^{-5/3}$). (B–D) Time-dependent shell averaged concentration spectrum calculated using the fraction f of the genetic mixture, for $Da = 0.1$ (B), $Da = 0.1$ with exponential rescaling of time (C) and $Da = 10$ (D). Selected time points. All time scales are given in the time scale of reproduction $1/\mu$.

In Fig. 4 B and D, we show the shell-averaged concentration spectrum of the transient dynamics for genetic mixtures with $Da = 0.1$ and 10 at different time points in the evolution of a circular disc inoculation, averaged over $N = 100$ runs with different flow fields. As the final state of an antagonistic mixture is an absorbing state with $f = 0$ or $f = 1$, all spatial fluctuations eventually vanish, causing the spectra to converge to zero in the long time limit. However, the transient dynamics depends strongly on the Damköhler number. Larger Damköhler numbers cause short wavelength fluctuations to get more strongly damped. Furthermore, for large Damköhler numbers, after an initial continuous reduction of the amplitude, the whole spectrum disappears quite fast around the fixation time. This abrupt disappearance reflects the fact that for large Da , fixation is reached largely by the growth and shrinkage of domains. For lower Damköhler numbers, however, the domains get mixed, and the system is more homogeneous already in the transient regime. This homogenization is seen more clearly when comparing the concentration spectrum of the genetic mixture to that of a passive scalar.

To highlight this relation, in Fig. 4C, we exponentially rescale in time the spectrum of the $Da = 0.1$ genetic mixture, which shows good collapse at late times, similar to that of the passive scalar. This collapse can be understood through a simple linearized analysis about one of the final absorbing states, valid for low Damköhler numbers and in the long time limit. Upon writing $\psi(x, t) = f(x, t) - f^*$, we obtain $(\partial_t + \mathbf{v} \cdot \nabla)\psi = D\nabla^2\psi - \kappa\psi$, where $\kappa = \mu(\sigma \pm \delta/2)$ for $f^* = 0$ or $f^* = 1$. The transformation $\Psi(x, t) = \exp(\kappa t)\psi(x, t)$ converts this linear dynamics to that of an advected passive scalar, namely $(\partial_t + \mathbf{v} \cdot \nabla)\Psi = D\nabla^2\Psi$, thus demonstrating the suggested equivalence.

Discussion

The growth of killer microbe strains in a turbulent environment warrants an unusual combination of conflicting tendencies — biological antagonism that actively tries to segregate different

strains and turbulent stirring that forces intermingling of the antagonistic populations. A key ingredient in our work is the presence of nonreciprocal ($\alpha \neq \beta$) and inhibitory ($\alpha, \beta < 0$) interactions in the growth rates of the organisms, making the system a kind of active matter (18). Our analysis highlights the role of nucleation thresholds in fixation and demonstrates how turbulent mixing strongly dictates which strain survives (or goes extinct), when it does so, and how its dynamics evolves spatially.

Range expansions of genetically engineered microbes, e.g., antagonistic yeast, growing on a stirred liquid substrate (21, 37) would be an ideal experimental platform to test our results. For marine phytoplankton with typical growth rates $\mu \sim 0.5$ to 1 d^{-1} and eddy turnover times $\tau_{\text{eddy}} \sim 5 \text{ min}$ to $\gtrsim 50 \text{ d}$ (on a range of spatial scales, ~ 0.1 to 100 km) (3, 8), a wide range of $Da \sim 10^{-3}$ to 10^4 is possible, suggesting our results may be relevant for understanding microbial population dynamics in the ocean. Further work incorporating 3D and compressible flows (2), demographic noise (22, 38, 39), multispecies interactions (40), pattern formation mechanisms (23, 24, 41), etc., is needed to understand the applicability of our results to biologically realistic microbial communities.

Our work also has implications for chemically reacting mixtures. In the limit of reciprocal interactions ($\alpha = \beta$, so $\delta = 0$), our model (Eqs. 1 and 2) reduces to similar autocatalytic models describing the synthesis of chiral biomolecules and the origins of biological chirality (42–44). Turbulent mixing is known to speed up the attainment of a fully homochiral state in chemical systems (45, 46) and has been suggested to play a role in dictating the handedness of prebiotic mixtures on distant planets (44, 47). Our results suggest a generalization to mixtures near their carrying capacity. Upon setting $\delta \rightarrow 0$ in Eq. 12, we predict a flow-enhanced critical fraction of $f_c = 1/2 + 2\pi D t_{\text{mix}}/L^2 + \mathcal{O}(\delta)$, i.e., the strain initialized as a droplet acquires an effective disadvantage from fluid mixing. This surprising asymmetry highlights the crucial role of interfaces and curvature in antagonistic mixtures

that get penalized by a chemical line tension but are amplified by fluid shear, suggesting an extraordinarily sensitive dependence of the long-term homochiral state on random fluctuations and geometry of the initial condition (43).

Materials and Methods

Here we provide additional details for numerically generating the flow field. Further details on the model, theoretical calculations, and analysis are provided in [SI Appendix](#).

Generation of the Flow Fields. We use a pseudospectral method for solving the Navier–Stokes equation in a 3D lattice with periodic boundary conditions with random forcing at long scales. In all our simulations, we have chosen the same resolution ($N = 128$ grid points for a system size with $L = 2\pi$) as for the numerical solver for the advected reaction–diffusion equations later. However, in this work, we focus on the flow of a 2D slice originating from the 3D flow field. This choice is motivated by the fact that many oceanographic micro-organisms control their buoyancy and live in a height-selected layer of the ocean; see refs. 3 and 2. By taking the 2D slice, we are generally left with a compressible flow. In this work, however, we restrict ourselves to the easier situation of an incompressible flow for simplicity, leaving the interesting effects of compressibility on the mixing of antagonistic populations for future work. Following ref. 48, we obtain the 2D incompressible part of the flow field \mathbf{v} by projecting its Fourier transform $\tilde{\mathbf{v}}$ via

$$\mathbf{v}_{\text{incom.}} = \mathcal{F}^{-1} \left(\tilde{\mathbf{v}} - \frac{\mathbf{k}(\mathbf{k} \cdot \tilde{\mathbf{v}})}{|\mathbf{k}|^2} \right), \quad [15]$$

where $\mathcal{F}^{-1}(\mathbf{x})$ denotes the inverse Fourier transform of \mathbf{x} , and \mathbf{k} is the frequency variable. Note that with this projection, we insure $\nabla \cdot \mathbf{v}_{\text{incom.}} = 0$, because $\mathbf{k} \cdot \tilde{\mathbf{v}}_{\text{incom.}} = \mathbf{k} \cdot \tilde{\mathbf{v}} - \mathbf{k} \cdot \tilde{\mathbf{v}}$, where $\tilde{\mathbf{v}}_{\text{incom.}}$ is the Fourier transform of the incompressible flow field $\mathbf{v}_{\text{incom.}}$. The latter is just called \mathbf{v} in the main text.

Data, Materials, and Software Availability. Data and scripts to reproduce our results have been published in Zenodo (49). All other data are included in the article and/or [supporting information](#).

ACKNOWLEDGMENTS. We acknowledge Martijn Dorrestijn for his contribution in the early stages of this project. D.R.N. acknowledges F. Ozturk for fruitful discussions. J.B. and D.R.N. acknowledge support from the Harvard Materials Research Science and Engineering Center through NSF Grant DNR-2011754. J.B. thanks the German Research Foundation for financial support through the DFG Project BA 8210/1-1. S.S. acknowledges illuminating discussions during the “Anti-Diffusion in Multiphase and Active Flows” hosted by the Isaac Newton Institute for Mathematical Sciences, Cambridge, supported by the EPSRC Grant EP/R014604/1.

Author affiliations: ^aDepartment of Physics, Harvard University, Cambridge, MA 02138; ^bSino-Europe Complex Science Center, School of Mathematics, Northwestern University of China, Shanxi 030051, Taiyuan, China; ^cDepartment of Physics and Istituto Nazionale di Fisica Nucleare, University of Rome Tor Vergata, Rome I-00133, Italy; ^dDepartment of Physics, University of Michigan, Ann Arbor, MI 48109; ^eDepartment of Applied Physics and Science Education, Eindhoven University of Technology, Eindhoven 5600 MB, The Netherlands; and ^fConsiglio Nazionale delle Ricerche - Istituto per le Applicazioni del Calcolo, Rome I-00185, Italy

Author contributions: J.B., R.B., D.R.N., S.S., and F.T. designed research; J.B., R.B., D.R.N., S.S., and F.T. performed research; J.B., R.B., D.R.N., S.S., and F.T. analyzed data; J.B. performed simulations, analytic calculations, and data analysis; and J.B., R.B., D.R.N., S.S., and F.T. wrote the paper.

1. D. A. Siegel, T. DeVries, I. Cetinić, K. M. Bisson, Quantifying the ocean’s biological pump and its carbon cycle impacts on global scales. *Annu. Rev. Mar. Sci.* **15**, 329–356 (2023).
2. R. Benzi, D. R. Nelson, S. Shankar, F. Toschi, X. Zhu, Spatial population genetics with fluid flow. *Rep. Prog. Phys.* **85**, 096601 (2022).
3. A. Martin, Phytoplankton patchiness: The role of lateral stirring and mixing. *Prog. Oceanogr.* **57**, 125–174 (2003).
4. G. Károlyi, Á. Péntek, I. Scheuring, T. Tél, Z. Toroczkai, Chaotic flow: The physics of species coexistence. *Proc. Natl. Acad. Sci. U.S.A.* **97**, 13661–13665 (2000).
5. F. d’Ovidio, S. De Monte, S. Alvain, Y. Dandonneau, M. Lévy, Fluid dynamical niches of phytoplankton types. *Proc. Natl. Acad. Sci. U.S.A.* **107**, 18366–18370 (2010).
6. A. D. Barton, S. Dutkiewicz, G. Flierl, J. Bragg, M. J. Follows, Patterns of diversity in marine phytoplankton. *Science* **327**, 1509–1511 (2010).
7. D. J. McGillicuddy Jr, Mechanisms of physical–biological–biogeochemical interaction at the oceanic mesoscale. *Annu. Rev. Mar. Sci.* **8**, 125–159 (2016).
8. A. Mahadevan, The impact of submesoscale physics on primary productivity of plankton. *Annu. Rev. Mar. Sci.* **8**, 161–184 (2016).
9. P. Villa Martín, A. Buček, T. Bourguignon, S. Pigolotti, Ocean currents promote rare species diversity in protists. *Sci. Adv.* **6**, eaaz9037 (2020).
10. P. Perlekar, R. Benzi, D. R. Nelson, F. Toschi, Population dynamics at high Reynolds number. *Phys. Rev. Lett.* **105**, 144501 (2010).
11. S. Pigolotti, R. Benzi, M. H. Jensen, D. R. Nelson, Population genetics in compressible flows. *Phys. Rev. Lett.* **108**, 128102 (2012).
12. S. Pigolotti et al., Growth, competition and cooperation in spatial population genetics. *Theor. Popul. Biol.* **84**, 72–86 (2013).
13. A. Plummer, R. Benzi, D. R. Nelson, F. Toschi, Fixation probabilities in weakly compressible fluid flows. *Proc. Natl. Acad. Sci. U.S.A.* **116**, 373–378 (2019).
14. A. Plummer et al., Oceanic frontal divergence alters phytoplankton competition and distribution. *J. Geophys. Res. Oceans* **128**, e2023JC019902 (2023).
15. G. J. Doucet, Interactions between bacteria and harmful algae: A review. *Nat. Toxins* **3**, 65–74 (1995).
16. R. A. Long, F. Azam, Antagonistic interactions among marine pelagic bacteria. *Appl. Environ. Microbiol.* **67**, 4975–4983 (2001).
17. J. B. Martiny, L. Riemann, M. F. Marston, M. Middelboe, Antagonistic coevolution of marine planktonic viruses and their hosts. *Annu. Rev. Mar. Sci.* **6**, 393–414 (2014).
18. O. Hallatschek et al., Proliferating active matter. *Nat. Rev. Phys.* **5**, 407–419 (2023).
19. S. Rouhani, N. Barton, Speciation and the “shifting balance” in a continuous population. *Theor. Popul. Biol.* **31**, 465–492 (1987).
20. M. O. Lavrentovich, D. R. Nelson, Nucleation of antagonistic organisms and cellular competitions on curved, inflating substrates. *Phys. Rev. E* **100**, 042406 (2019).
21. A. Giometto, D. R. Nelson, A. W. Murray, Antagonism between killer yeast strains as an experimental model for biological nucleation dynamics. *eLife* **10**, e62932 (2021).
22. J. F. Crow, *An Introduction to Population Genetics Theory* (Scientific Publishers, 2017).
23. S. A. Levin, L. A. Segel, Pattern generation in space and aspect. *SIAM Rev.* **27**, 45–67 (1985).
24. J. D. Murray, *Mathematical Biology. II: Spatial Models and Biomedical Applications* (Springer, 2003), vol. 18.
25. B. Legras, P. Santangelo, R. Benzi, High-resolution numerical experiments for forced two-dimensional turbulence. *Europhys. Lett.* **5**, 37 (1988).
26. U. Frisch, *Turbulence: The Legacy of AN Kolmogorov* (Cambridge University Press, 1995).
27. Z. Neufeld, E. Hernández-García, *Chemical and Biological Processes in Fluid Flows: A Dynamical Systems Approach* (World Scientific, 2009).
28. P. C. Hohenberg, B. I. Halperin, Theory of dynamic critical phenomena. *Rev. Mod. Phys.* **49**, 435–479 (1977).
29. R. Ruiz, D. R. Nelson, Turbulence in binary fluid mixtures. *Phys. Rev. A* **23**, 3224 (1981).
30. S. Berti, G. Boffetta, M. Cencini, A. Vulpiani, Turbulence and coarsening in active and passive binary mixtures. *Phys. Rev. Lett.* **95**, 224501 (2005).
31. P. Perlekar, R. Benzi, H. J. H. Clercx, D. R. Nelson, F. Toschi, Spinodal decomposition in homogeneous and isotropic turbulence. *Phys. Rev. Lett.* **112**, 014502 (2014).
32. K. R. Sreenivasan, Turbulent mixing: A perspective. *Proc. Natl. Acad. Sci. U.S.A.* **116**, 18175–18183 (2018).
33. J. O. Hinze, Fundamentals of the hydrodynamic mechanism of splitting in dispersion processes. *AIChE J.* **1**, 289–295 (1955).
34. H. Tanaka, H. A. Stone, D. R. Nelson, Spatial gene drives and pushed genetic waves. *Proc. Natl. Acad. Sci. U.S.A.* **114**, 8452–8457 (2017).
35. R. Durrett, S. Levin, The importance of being discrete (and spatial). *Theor. Popul. Biol.* **46**, 363–394 (1994).
36. B. I. Shraiman, E. D. Siggia, Scalar turbulence. *Nature* **405**, 639–646 (2000).
37. S. Atis, B. T. Weinstein, A. W. Murray, D. R. Nelson, Microbial range expansions on liquid substrates. *Phys. Rev. X* **9**, 021058 (2019).
38. A. J. McKane, T. J. Newman, Predator–prey cycles from resonant amplification of demographic stochasticity. *Phys. Rev. Lett.* **94**, 218102 (2005).
39. M. Pineda-Krch, H. J. Blok, U. Dieckmann, M. Doebeli, A tale of two cycles-distinguishing quasi-cycles and limit cycles in finite predator–prey populations. *Oikos* **116**, 53–64 (2007).
40. M. T. Pearce, A. Agarwala, D. S. Fisher, Stabilization of extensive fine-scale diversity by ecologically driven spatiotemporal chaos. *Proc. Natl. Acad. Sci. U.S.A.* **117**, 14572–14583 (2020).
41. A. Martinez-Calvo, N. S. Wingreen, S. S. Datta, Pattern formation by bacteria–phage interactions. *bioRxiv* [Preprint] (2023). <https://doi.org/10.1101/2023.09.19.558479> (Accessed 1 August 2024).
42. F. C. Frank, On spontaneous asymmetric synthesis. *Biochim. Biophys. Acta* **11**, 459–463 (1953).
43. F. Jafarpour, T. Biancalani, N. Goldenfeld, Noise-induced mechanism for biological homochirality of early life self-replicators. *Phys. Rev. Lett.* **115**, 158101 (2015).
44. A. Brandenburg, T. Multamäki, How long can left and right handed life forms coexist? *Int. J. Astrobiol.* **3**, 209–219 (2004).
45. D. K. Kondepudi, R. J. Kaufman, N. Singh, Chiral symmetry breaking in sodium chlorate crystallization. *Science* **250**, 975–976 (1990).
46. Y. Saito, H. Hyuga, Colloquium: Homochirality: Symmetry breaking in systems driven far from equilibrium. *Rev. Mod. Phys.* **85**, 603 (2013).
47. F. Frank, On spontaneous asymmetric synthesis. *Biochim. Biophys. Acta* **11**, 459–463 (1953).
48. P. Perlekar, R. Benzi, D. R. Nelson, F. Toschi, Cumulative compressibility effects on slow reactive dynamics in turbulent flows. *J. Turbul.* **14**, 161–169 (2013).
49. J. Bauermann, R. Benzi, D. R. Nelson, S. Shankar, F. Toschi, Code and data for “Turbulent mixing controls fixation of growing antagonistic populations.” Zenodo. <https://zenodo.org/records/14719305>. Deposited 22 January 2025.